Wireless Nano Irradiance Meter Based on Upconversion Luminescence Lifetime

Alejandro Casillas-Rubio, Marco Laurenti, Juan Pedro Cascales, Oscar G. Calderón, Diego Mendez-Gonzalez,* and Sonia Melle**

Measuring light irradiance, or power density, within a material is essential for ensuring the precision, efficiency, and safety of light-based technologies, such as photodynamic therapies, optical sensing, and material processing. However, this task becomes particularly challenging in scenarios involving highly scattering or absorbing media, dynamic systems with varying properties, or confined and hardly accessible compartments. These challenges can be addressed by using colloidal luminescent nanomaterials with luminescence lifetimes strongly dependent on excitation irradiance. Building on this, an upconversion lifetime-based Nano Irradiance Meter (nIM) is proposed, employing, on SrYb^{3+}F$_5$:Tm$^{3+}_{0.5\%}$@CaF$_2$ upconverting nanoparticles. This nIM operates within the first biological window and allows the direct estimation of laser irradiance, without prior knowledge of the area illuminated by the excitation beam. The feasibility of the sensor is validated through a calibration process, correlating the lifetime of the 770 nm upconversion luminescence of Tm^{3+} ions with the 967 nm excitation irradiance. The sensor achieved a sensitivity of 0.9% W^{-1} cm^2 at low irradiances (≈17 W cm^{-2}) and 0.008% W^{-1} cm^2 at high irradiances (≈5 kW cm^{-2}), surpassing previously reported results based on ratiometric luminescence approaches. Finally, its robust performance under real-life conditions across various media is demonstrated.

1. Introduction

The more we learn about the intriguing light-matter interactions, the more we are encouraged to explore their limits, accelerating the incorporation of novel optical technologies to industry, medicine, energy and other fields that ultimately impact our daily lives. Photolithography, 3D-printing with photo-curable resins, optical sensors, laser surgery, and even novel biomedical procedures such as photodynamic and photothermal therapies, or luminescent nanothermometry, are just some fascinating examples of the incredibly fast development of such technologies.

To gain full control over these technologies, by ensuring safety, optimal performance, and adequate quality standards, the measurement and assessment of light irradiance is unavoidably a crucial step. Monitoring the local irradiance within a material allows us to objectively deduce whether the amount of energy transferred to the material per unit area and time (i.e., power density) is sufficient to initiate a specific process. Additionally, it enables the study of light propagation through the material and the investigation of light-matter interaction.

Irradiance or power density can be measured using various methods, with photodiode sensors and thermopile sensors being among the most convenient and widely used options (see **Figure 1**). These devices work by transforming the absorbed light into an electrical signal, being this related to the absorbed power. Nevertheless, irradiance values still need to be worked out by carefully characterizing the area of the detector that is being illuminated, which can be challenging and time-intensive. In addition, the bulky and rigid nature of these sensors, make them unsuitable for optical applications where irradiance needs to be monitored within complex, hardly accessible, or small and confined media such as light-scattering materials like polymers or biological tissues, and millimetric to submicrometric compartments like microfluidic devices, tissues, cells, porous media, etc.

Interestingly, nascent optical therapies such as light-triggered drug delivery, or photodynamic and photothermal therapies, can greatly benefit from local irradiance measurements, as a means to monitor and ensure treatment safety, effectiveness and reproducibility under standardized in situ illumination conditions.[1,2] In fact, measuring light dosimetry non-invasively during treatments such as photodynamic therapy is considered as an essential parameter dictating treatment efficacy[1,3] while being widely regarded as a very ambitious yet unmet goal. In this regard,

A. Casillas-Rubio, O. G. Calderón, S. Melle
Department of Optics
Complutense University of Madrid
Madrid E-28037, Spain
E-mail: oscargc@ucm.es; smellehe@ucm.es

M. Laurenti, J. P. Cascales, D. Mendez-Gonzalez
Department of Chemistry in Pharmaceutical Sciences
Complutense University of Madrid
Madrid E-28040, Spain
E-mail: diegomen@ucm.es

The ORCID identification number(s) for the author(s) of this article can be found under https://doi.org/10.1002/adom.202500093

DOI: 10.1002/adom.202500093

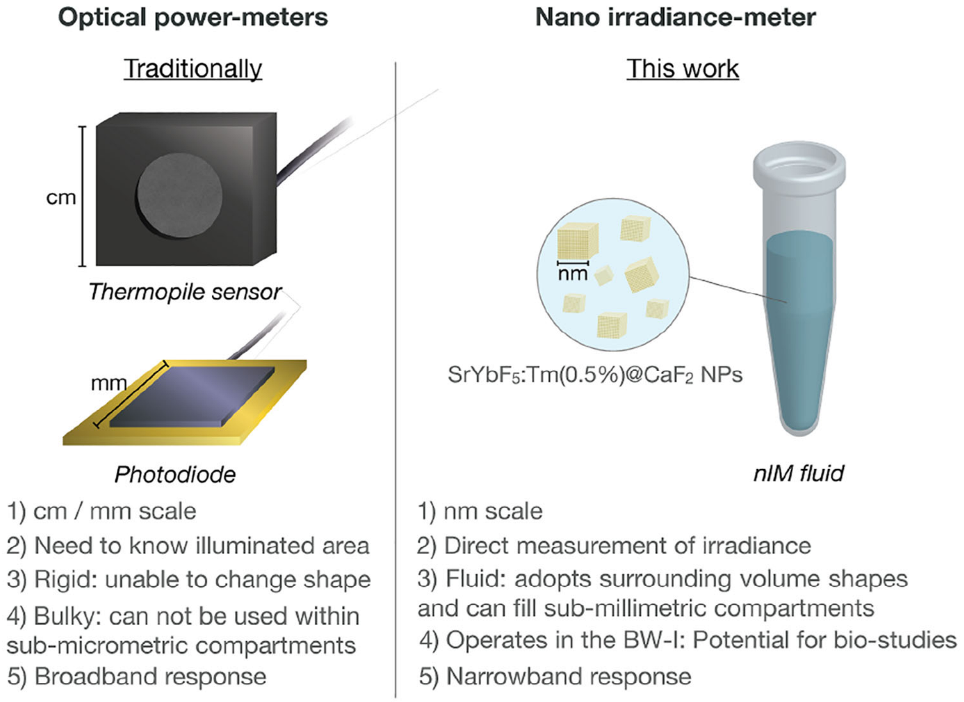

Figure 1. (left) Schematic representation of common methods for measuring light irradiance through power detection, including photodiodes and thermopile sensors. (right) Diagram of the proposed wireless nano-irradiance meter, which utilizes a solution of lanthanide-doped upconverting nanoparticles and exploits the dependence of upconversion luminescecne lifetime on excitation irradiance. The main advantages and limitations of these sensors are shown.

using nanoparticle dispersions featuring power-dependent luminescent responses, which can diffuse and fill submicrometric cavities, while adopting different shapes due to their fluidity, would constitute an invaluable tool to study and monitor irradiance and light propagation in situations where this is not currently possible.

To our knowledge, previous works using changes in luminescence to estimate the incident irradiance are scarce and primarily based on luminescence intensity ratiometric measurements.[2,4,5] For example, Marciniak et al. used the Cr^{3+} light-to-heat conversion capability, and the intensity ratio between the $^4T_{2(g)}$ and $^2E_{(g)}$ levels, induced by temperature changes, to relate the local temperature generated by Cr^{3+} doped-$GdAl_3(BO_3)_4$ to the excitation power. This approach allowed them to estimate the incident laser power indirectly.[4] In a similar fashion, by using $NaYF_4$:Gd^{3+}, Yb^{3+}, Er^{3+} nanostructures, Hernández-Álvarez et al. employed the Er^{3+} intensity ratio of the green emission bands located at 525 and 550 nm, which are thermally coupled acting as a Boltzmann thermometer, to relate the local temperature feedback provided by these nanostructures with the incident excitation power.[5] Finally, Costa Martins et al. have discovered a way to independently monitor excitation power and temperature using $NaGdF_4$/$NaGdF_4$:Yb^{3+}, Er^{3+}/$NaGdF_4$ nanoparticles. While absolute temperature can be read using the intensity ratio between $^2H_{11/2} \rightarrow {}^4I_{15/2}$ and $^4S_{3/2} \rightarrow {}^4I_{15/2}$ Er^{3+} emissions bands, the overlapping between $^2H_{9/2} \rightarrow {}^4I_{13/2}$ and $^4S_{3/2} \rightarrow {}^4I_{15/2}$ bands can make its accurate determination difficult. By deconvoluting this spectral region into different gaussians corresponding to the distinct transitions, they were able to isolate the ratiometric Boltzmann thermometer from the $^2H_{9/2} \rightarrow {}^4I_{13/2}$ transition, which was power dependent and served to monitor the excitation power that reached the nanoparticles.[2]

Whereas these strategies are suitable to quantify light irradiance in controlled conditions, they can be biased when applied in different and complex environments. For example, both the shape and intensity of emission spectra can be easily distorted and attenuated when measured in complex media (e.g., tissue), due to light absorption and scattering, making the readouts obtained by the described systems misleading.[6–9] These spectral changes may not only be static, but dynamic when the nanomaterial concentration is changing due to diffusion, or when properties of the media are modified with the variation of external parameters such as temperature.[10–12] As a result, translating these strategies to these scenarios present important difficulties. Nevertheless, they could be circumvented using a robust magnitude insensitive to these effects, which enables the unbiased monitoring of irradiance. Luminescence lifetime could be a feasible alternative, due to its reliability even in complex media.[13–16] Thus, although challenging, finding a colloidal nanomaterial whose luminescence lifetime exhibits a strong power-dependent response would provide a new class of nano-powermeter, capable of providing accurate feedback of local irradiance in currently impossible situations.

In this regard, lanthanide-doped upconverting nanoparticles (UCNPs) are promising candidates to explore[17] because: i) their anti-Stokes emissions enable luminescence monitoring even in complex media where autofluorescence could interfere with conventional fluorophores,[18] ii) UCNPs exhibit exceptional optical stability, being unaffected by blinking or photobleaching,[19] iii) their lanthanide composition provides

Table 1. Comparison between different luminescence-based irradiance estimation methods.

Material	$SrYb_{0.995}F_5$: $Tm_{0.005}$ @CaF_2	$NaGdF_4$ @$NaGd_{0.78}F_4$:$Yb_{0.2}$;$Er_{0.02}$ @$NaGdF_4$	Cr^{3+}-doped $GdAl_3(BO_3)_4$ (Different Cr^{3+} doping of 1%, 5% and 10%)	β-$NaY_{0.78}F_4$:$Gd_{0.1}$;$Yb_{0.1}$;$Er_{0.02}$
Size	16 nm	35 nm	c.a. 400 nm	Rod shape: 50-100 nm (width) 1 μm (length)
State	Dispersed NPs (fluid)	Dispersed NPs (fluid)	Dried solid powder	Dried solid pellet (260 μm width)
Working principle	Luminescence lifetime	Emission intensity ratio	Emission intensity ratio	Emission intensity ratio
Biased by light scattering	No	Partially†	Partially†	Partially†
Biased by light absorption	No	Partially†	Partially†	Partially†
Biased by temperature	No (up to 40 °C); slight at 50 °C	Yes, requires mathematical treatment	Yes	Yes
Biased by autofluorescence	No (large anti-Stokes-shifted emissions)	No (large anti-Stokes-shifted emissions)	Likely (Stokes-shifted emissions)	No (large anti-Stokes-shifted emissions)
Photobleaching	No (Rare Earth-doped inorganic host)	No (Rare Earth-doped inorganic host)	Unlikely (Cr^{3+}-doped inorganic host)	No (Rare Earth-doped inorganic host)
Relative Sensitivity (Sr)	0.89–0.0046 % W^{-1} cm^2 (17–15541 W cm^{-2})	0.5–0.08 % W^{-1} cm^2 (29–138.8 W cm^{-2})	0.07–10^{-4} % W^{-1} cm^2 (1.2–3650 W cm^{-2}; 10% Cr^{3+}) 7–2.4 × 10^{-3} % W^{-1} cm^2 (1.2–4356 W cm^{-2}; 1% Cr^{3+})	0.46–0.1 % W^{-1} cm^2 (0.27–930 W cm^2)
Tested dynamic range	17–15541 W cm^{-2}	29–138.8 W cm^{-2}	1.2–3650 W cm^{-2} (10% Cr^{3+}) 1.2–4356 W cm^{-2} (1% Cr^{3+})	c.a. 0.27–930 W cm^{-2}
Ref.	**This work**	2	4	5

† Less than other single band emission intensity sensors.

long-lived energy states and large luminescence lifetimes (μs to ms), which can be easily monitored with relatively simple and inexpensive instrumentation,[20,21] iv) their non-linear optical behavior makes them highly sensitive to changes in excitation irradiance,[18] v) UCNPs exhibit power-dependent lifetimes[22–25] showing varied behavior depending on factors such as nanoparticle size and structure, excitation irradiance range, doping ion composition, and the state (powder or solution). In a recent study, we demonstrated that the luminescence lifetime of the Er^{3+} green emission band is directly correlated with the incident fluence (irradiance for a fixed excitation pulse length) of the excitation source.[26] This is the result of the complex dynamics of the upconversion process, arising from the power-dependent population of different energy levels of nearby ions that are inter-connected through multiple energy transfer processes.

In this work we have developed and assessed a novel kind of powermeter: an upconversion lifetime-based Nano Irradiance Meter (nIM) composed of $SrYb^{3+}F_5$:$Tm^{3+}_{0.5\%}$@CaF_2 UCNPs. This wireless nIM offers multiple advantages compared with bulk power meters or previously reported nano power meters based on monitoring UCNPs' luminescence spectra[2,4,5,27] (see **Table 1**): i) it provides an absolute value of excitation irradiance without the need to measure excitation beam area, even in complex media; ii) using upconversion lifetime as the correlating parameter to irradiance avoids biases during monitoring in scattering or optically absorbent media, as well as biases introduced by UCNP concentration and distribution; iii) it operates in the first biological window (BW-I, ≈700–950 nm), a spectral region where tissues are more optically transparent, making it promising for in vivo and ex vivo studies; iv) as a suspension of colloidal UCNPs, its fluid nature enables it to adopt any shape, diffuse through porous media, and fill sub-millimetric compartments, thereby allowing measurement of local irradiances within these environments (see Figure 1). The successful application of these nIMs using real tissue slices highlights the potential of this technology to remotely monitor local irradiances and address current limitations in photodynamic therapy or emerging technologies such as nanothermometry.

2. Results and Discussion

By using the thermal decomposition method, we firstly synthesized $SrYbF_5$:$Tm^{3+}_{0.5\%}$ UCNPs cores, featuring a mean diameter of 4.3 ± 0.5 nm (see the schematic representation and the corresponding high-resolution transmission electron microscopy (HR-TEM) in **Figure 2**A-i and A-ii, respectively). After that, we enlarged these cores by epitaxial growth, using the core $SrYbF_5$:$Tm^{3+}_{0.5\%}$ UCNPs as seeds, and a precursor solution, with the same composition as that used for the core synthesis, as growth solution (Figure 2B-i). The size of the resulting UCNPs was 8.0 ± 2.0 nm (see HR-TEM in Figure 2B-ii). Finally, these enlarged core UCNPs were coated with a protective CaF_2 inactive shell to reduce surface quenching and enhance their emission (Figure 2C-i). HR-TEM image analysis of the CaF_2 coated

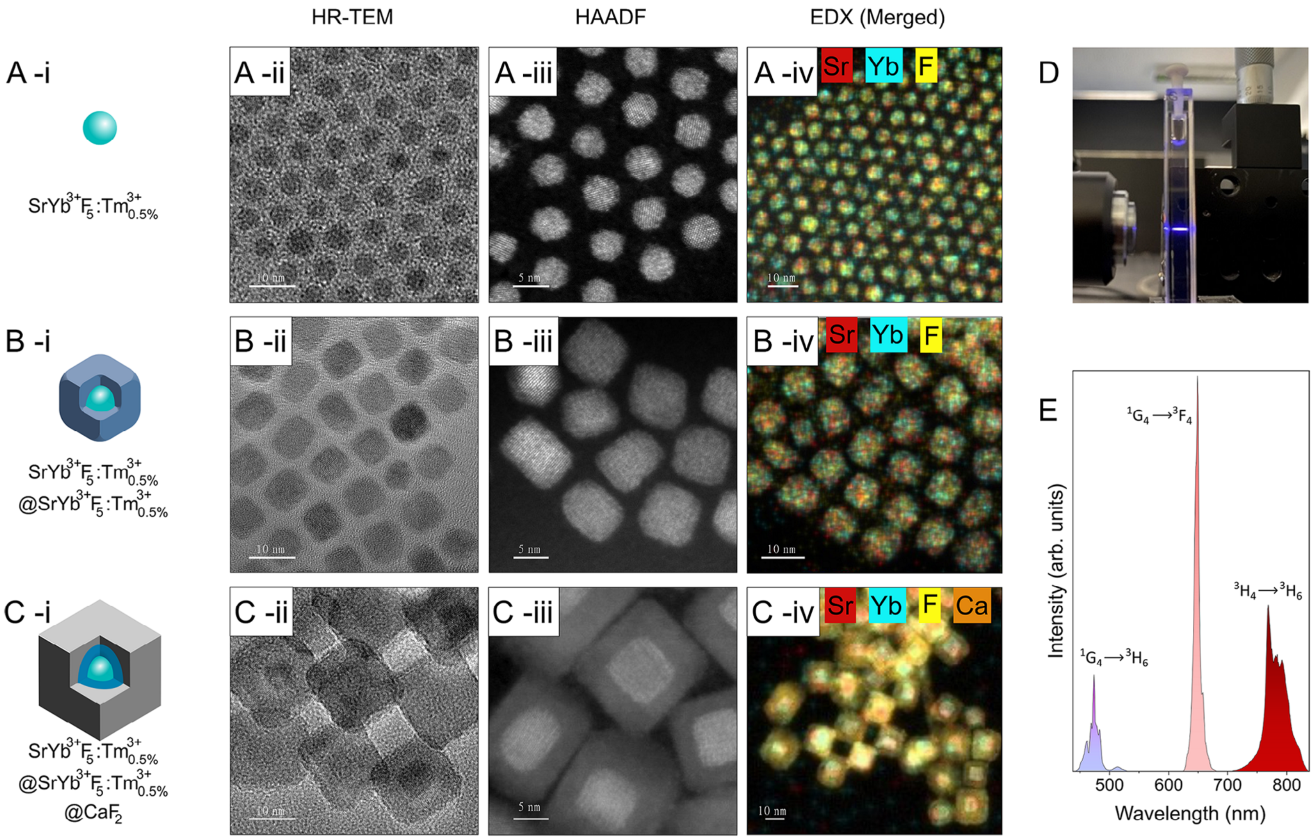

Figure 2. Comprehensive structural and compositional analysis of the UCNPs along the different synthetic steps. (A-i), (B-i), and (C-i) show a schematic representation of the $SrYbF_5$:$Tm^{3+}_{0.5\%}$ core, $SrYbF_5$:$Tm^{3+}_{0.5\%}$@$SrYbF_5$:$Tm^{3+}_{0.5\%}$ enlarged core, and $SrYbF_5$:$Tm^{3+}_{0.5\%}$@$SrYbF_5$:$Tm^{3+}_{0.5\%}$@CaF_2 core-shell UCNPs, respectively. (A-ii), (B-ii), and (C-ii) are HR-TEM images of the synthesized nanoparticles (scale bar = 10 nm). (A-iii), (B-iii), and (C-iii) show the HAADF images of the different nanoparticles (scale bar = 5 nm). (A-iv), (B-iv), and (C-iv) represent the merged EDX analysis for Ca (only C-iv), Sr, Yb, and F; (scale bar = 10 nm). (D) Image showing the upconversion emission from a cuvette containing a 1mg mL^{-1} dispersion of core@shell UCNPs in toluene under 967 nm NIR laser excitation (380 W cm^{-2}). (E) Upconversion luminescence emission spectrum from the same dispersion under 967 nm NIR laser excitation (3 kW cm^{-2}).

UCNPs showed a diameter of 16.1 ± 2.7 nm (Figure 2C-ii). High-angle anular dark-field (HAADF) magnification of the core, enlarged core, and core-shell UCNPs are shown in Figure 2A-iii, B-iii, and C-iii, respectively. HAADF images clearly show the crystalline nature of the products through the different stages, and the core@shell structure of the final UCNPs (Figure 2C-iii). Compositional analyses of the UCNPs for Ca, Sr, Yb, and F are shown in Figure S1 (Supporting Information) while merged energy-dispersive X-ray spectroscopy (EDX) analysis can be seen in Figure 2A-iv, B-iv, and C-iv. These images confirm the presence of Sr, Yb, and F within the UCNPs structure in all synthetic steps, as well as the incorporation of Ca during the final CaF_2 shell growth (Figure 2C-iv). As opposed to our previous study,[26] in this work we decided to explore Tm^{3+}-doped UCNPs due to their emission within the BW-I, as well as for their ability to potentially initiate various processes such as photodynamic therapy (e.g., through their red and blue emissions) and photochemical reactions (e.g., blue and UV emissions), turning them potentially versatile multimodal platforms. Additionally, the $SrYbF_5$ matrix was chosen for its high quantum yield performance.[28] Figure 2D shows the visible emission of a 1 mg mL^{-1} colloidal dispersion of the resulting $SrYb^{3+}F_5$:$Tm^{3+}_{0.5\%}$@$SrYb^{3+}F_5$:$Tm^{3+}_{0.5\%}$@CaF_2 UCNPs in toluene when excited at 967 nm. In Figure 2E, the visible-near-infrared upconversion luminescence emission spectrum shows three emission bands from Tm^{3+} ions. A blue band with maximum at 474 nm, which corresponds to the $^1G_4 \rightarrow {}^3H_6$ transition, a red band with maximum at 650 nm corresponding to the $^1G_4 \rightarrow {}^3F_4$ transition, and a near-infrared (NIR) band with maximum at 770 nm corresponding to the $^3H_4 \rightarrow {}^3H_6$ transition (see diagram with energy levels in Figure 4A). $^1G_4$ and $^3H_4$ levels are populated via energy transfer from Yb^{3+} ions, which absorb the laser excitation and initiate the energy transfer process to Tm^{3+} ions, resulting in the described upconversion emissions. The upconversion nature of the process was further confirmed by analyzing the emission intensity of the 770 nm UCL band as a function of excitation irradiance, which revealed a power-law dependence with an exponent of approximately 1.2 (Figure S2, Supporting Information).

2.1. Proof of Concept

As mentioned in the Introduction, the complex dynamics of the upconversion process cause the upconversion luminescence

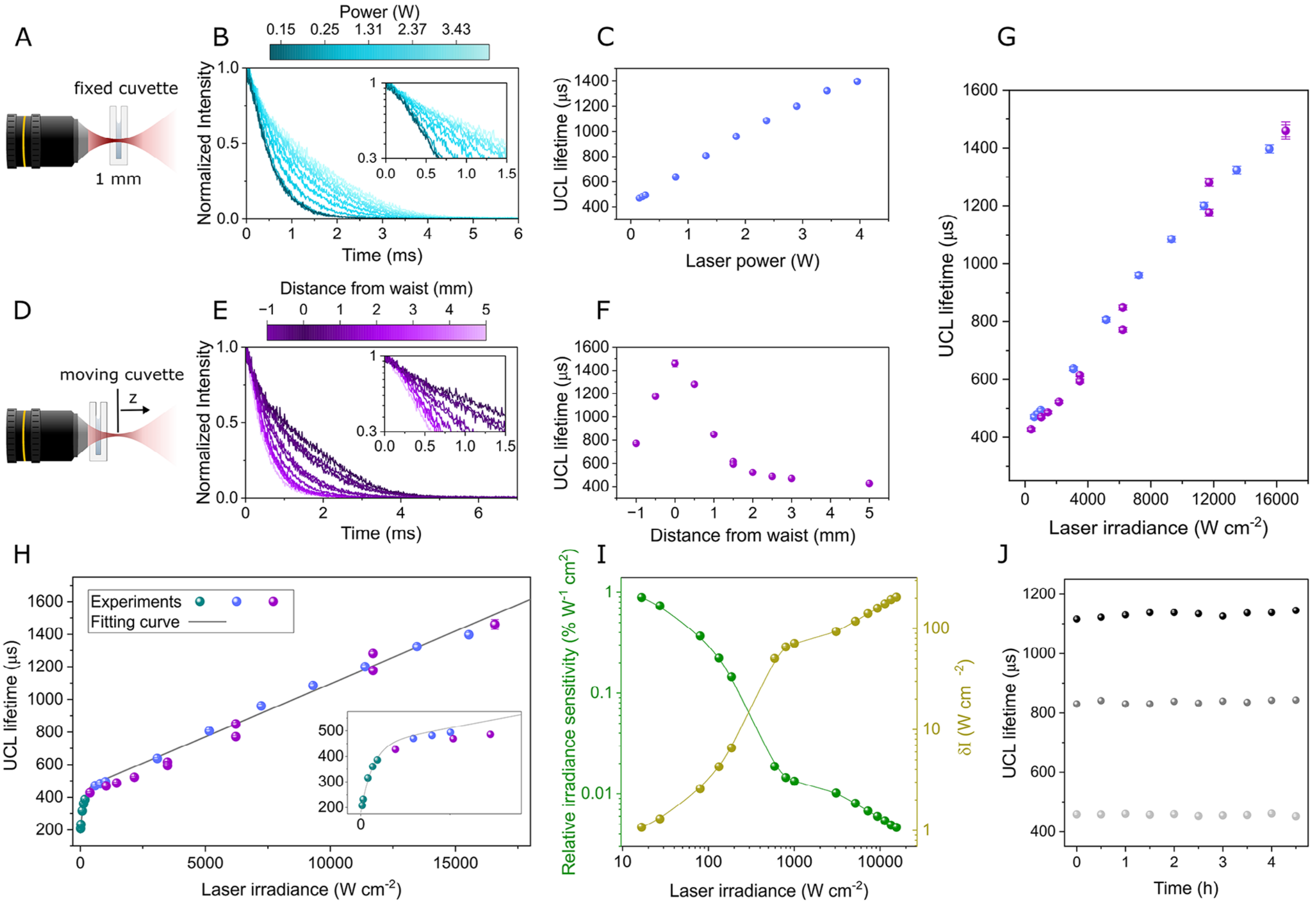

Figure 3. A) Schematic of the experimental procedure for measuring the UCL lifetime as a function of laser power mantaining the cuvette position at the beam waist. B) NIR 770 nm UCL decay curves for various excitation powers. The inset shows the initial decay of the UCL curves on a logarithmic y-axis. C) UCL lifetimes derived from the decay curves in (B) for different excitation powers. D) Schematic of the experimental procedure for measuring the UCL lifetime by varying the position of the cuvette while maintaining a fixed power of 4.22 W. E) NIR 770 nm UCL decay curves for different cuvette positions. The inset displays the initial decay of the UCL curves on a logarithmic y-axis. F) UCL lifetimes extracted from the decay curves in (E) for various cuvette positions. G) UCL lifetime from graphs (C) and (F) as a function of the laser irradiance. H) Same graph as in (G), with the addition of UCL lifetime measurements at lower irradiance levels, obtained using a 4x microscope objective and a 0.6 optical density filter along the excitation path (represented by bluish-green symbols). The solid line represents the analytical curve chosen to fit the experimental data, given by Equation (1), with fitting parameters $\tau_0 = 446.8$ µs, $A = -266.9$ µs, $\sigma = 132.6$ W cm^{-2}, and $m = 0.0649$ µs W^{-1} cm^{2}. The inset highlights the low irradiance regime. I) (left axis) Relative irradiance sensitivity S_r (from Equation (2)) and (right axis) irradiance resolution δI (from Equation (3)) as functions of laser irradiance. Lines in (I) are guides for the eye. J) The UCL lifetime measured under constant conditions for three excitation irradiances: 380, 6000, and 10570 W cm^{-2}, over 4.5 h, every half hour. We obtained mean lifetimes and standard deviations of 456.9 ± 2.9 µs, 836 ± 5.2 µs, and 1132.4 ± 8.8 µs, respectively, given relative errors below 1% ($\delta\tau/\tau = 0.64\%$, 0.63%, and 0.8%, respectively).

(UCL) lifetime to depend on the excitation power. This phenomenon could pave the way for a new type of nanopower sensor based on the interaction between two variables: the UCL lifetime and the excitation power. To explore this concept, we studied the 770 nm upconversion NIR emission band of Tm^{3+}-doped UCNPs, when excited by a 967 nm NIR pulse laser. The setup for performing the time-resolved luminescence measurements is shown in Figure S3 (Supporting Information).

A pulse width of 10 ms was chosen to enhance the effect of laser power on the UCL lifetime. This was chosen after testing various laser pulse widths (Figure S4, Supporting Information). A pulse repetition frequency of 20 Hz was selected to allow Tm^{3+} and Yb^{3+} ions to fully relax to the ground state before each subsequent excitation pulse, thereby avoiding pile-up effects.[29] The cuvette containing the UCNP solution was positioned at the laser beam waist (see **Figure 3**A). UCL lifetime was investigated by varying the laser power from 0.15 to 3.95 W. As shown in Figure 3B, the UCL decay curves become slower as the laser power increases, suggesting an increment of the luminescence lifetime. The UCL lifetime was determined by fitting the decay curves to an exponential function using a variable fitting window, as detailed in the Experimental Section. Additionally, to confirm the robustness of the results, we also calculated the lifetime by integrating the decay curves (area under the curve), which is equivalent to calculating the average decay time in the case of a multi-exponential function. This method yielded comparable lifetime values (Figure S5, Supporting Information). Figure 3C shows the resulting UCL lifetime values as a function of laser power, exhibiting a substantial increase of more than 200% with an almost linear trend across the measured range. This result is of paramount importance, as it establishes the basis for the development of wireless monitored power meter sensors with the potential to be incorporated into future bioapplications. To clarify the role of the beam spot size on the results, we measured the UCL decay curves by varying the position of the cuvette along the beam propagation axis (see schematic in Figure 3D) while maintaining a constant excitation power (4.22 W). The UCL decay curves and the corresponding UCL lifetime as a function of the cuvette position are shown in Figure 3E,F, respectively. The maximum UCL lifetime (1460 μs) was achieved when the sample was positioned at the beam waist. As the sample was moved away from this position, the UCL lifetime decreased, exhibiting a symmetrical behavior around the beam waist. This corresponds well to the symmetrical variation in spot size around the beam waist. These findings suggest that the variation in UCL lifetime is governed by laser irradiance, i.e., the laser power divided by the spot area. To further support this observation, we combined the lifetime measurements from Figure 3C,F and plotted them as a function of laser irradiance in Figure 3G. To achieve this, we first measured the laser beam diameter along the propagation axis using the knife-edge technique[30] (see Section S6, Supporting Information). A clear overlap between both experiments is observed in Figure 3G, demonstrating that the UCL lifetime is a direct reflection of the laser irradiance reaching the UCNP solution. This implies that the UCNPs presented in this work represent, to our knowledge, the first example of a nIM.

2.2. Calibration Curve

Figure 3G serves as a basis for establishing a calibration curve for the irradiance sensor. This calibration allows the direct estimation of laser irradiance, without prior knowledge of the area illuminated by the excitation beam. The irradiance values used in this work reached the order of kW cm^{-2}, exceeding those reported by Marciniak et al.,[4] whose sensor operated within a range of 1.2 to 4356 W cm^{-2} before saturating. To extend the operating range of our nanoirradiance meter to lower excitation irradiance levels, we modified our experimental setup by replacing the 10x microscope objective with a 4x objective and adding a neutral density filter with an optical density of 0.6 to the excitation path. These adjustments reduced the irradiance to the range of tens of W cm^{-2}, aligning with ranges used by other authors.[2,4,5] For example, Hernández-Álvarez et al.[5] used irradiances from 0.27 to 930 W cm^{-2} whereas Martins et al.[2] used irradiances from 29 to 138.8 W cm^{-2}, achieving a maximum relative irradiance sensitivity of 0.5% W^{-1} cm^2 at 29 W cm^{-2}.

Using the modified experimental setup, we measured the UCL decay curves while varying the laser power within the low irradiance regime. The corresponding UCL lifetime as a function of laser irradiance is shown in Figure 3H (bluish-green symbols), alongside the previous measurements. A continuous trend is observed, as highlighted in the inset of Figure 3H. At lower irradiance levels, the increase in UCL lifetime is much more pronounced, indicating greater sensitiviy in this range. The experimental data in Figure 3H provide a calibration curve for the nIM, with a working range spanning approximately three orders of magnitude, enabling the estimation of irradiance in the region where the UCNPs are located. This can be simply achieved by measuring the UCL lifetime and interpolating the data from Figure 3H. To simplify the characterization of the nIM, we also fit the experimental results from Figure 3H to an analytical function that accurately describes the relationship between UCL lifetime and laser irradiance. Specifically, we selected the following function:

$$\tau = \tau_0 + Ae^{-I/\sigma} + mI \tag{1}$$

which combines both exponential and linear components, resulting in an initial rapid increase followed by an approximately linear trend, aligning with the experimental results. Here, I represents the laser irradiance and τ is the UCL lifetime, while τ_0, A, σ, and m are fitting constants that adjust the model to the experimental data. The fitting parameters obtained were $\tau_0 = 446.8$ μs, $A = -266.9$ μs, $\sigma = 132.6$ W cm^{-2}, and $m = 0.0649$ μs W^{-1} cm^2. The resulting analytical curve is plotted as a solid line in Figure 3H.

To characterize the performance of the nIM, the relative irradiance sensitivity, S_r, was calculated using the following definition:

$$S_r = \frac{1}{\tau}\left|\frac{\partial \tau}{\partial I}\right| \tag{2}$$

Figure 3I (left axis) shows S_r as a function of laser irradiance. In the low irradiance regime, we achieved a sensitivity of 0.89% W^{-1} cm^2 at 17 W cm^{-2}, which surpasses the maximum sensitivity reported by Martins *et al.*[2] (0.5% W^{-1} cm^2 at 29 W cm^{-2}). In the high irradiances regime, Marcianik *et al.*[4] reported a relative sensitivity of 0.0024% W^{-1} cm^2 at 4.356 kW cm^{-2}, using $GdAl_3(BO_3)_4$:Cr^{3+}(1%) nanoparticles. In comparison, our study achieved a sensitivity four times higher, reaching 0.008% W^{-1} cm^2 under similar conditions. Thus, our proposed sensor simultaneously surpasses the previously reported relative sensitivities at both low and high irradiances with the same system. Table 1 presents a comparative summary of the main limitations, performance metrics, and key characteristics of previously reported systems alongside those of our nanosensor.

Additionally, nanosensor irradiance resolution, δI, was determined using the following equation:

$$\delta I = \frac{1}{S_r}\frac{\delta \tau}{\tau} \tag{3}$$

where $\delta\tau$ represents the uncertainty in determining the UCL lifetime. To estimate the relative lifetime error $\delta\tau/\tau$, we measured the UCL lifetime under constant experimental conditions over more than four hours and for three different irradiances (380, 6000, and 10570 W cm^{-2}) along the range of values used in the calibration curve. The results, shown in Figure 3J, demonstrate stable behavior. For all three curves, we obtained a relative lifetime error slightly below 1%. This value was then used to calculate the irradiance resolution δI from Equation (3) for the entire range of excitation irradiances. Figure 3I (right axis) shows δI as a function of laser irradiance. The results indicate that irradiance can be determined with a precision of approximately 1 W cm^{-2} at low irradiance levels, and around 100 W cm^{-2} at higher levels, corresponding to a relative uncertainty range of 5% to 1%, respectively.

To confirm that the operation of our proposed nanoirradiance meter is not influenced by temperature-related factors, we conducted time-resolved luminescence experiments using a temperature-controlled cuvette holder. We measured the UCL decay curves as a function of the laser irradiance at two different temperatures, 25 and 40 °C, and observed strikingly similar behavior (Figure S7, Supporting Information). This experiment demonstrates the reproducibility of the phenomenon, even at varying temperatures. Furthermore, to explore the robustness of the system under more extreme conditions outside the typical physiological range, we extended the temperature range from 4 to 50 °C at a fixed excitation irradiance (Figure S7, Supporting Information). This range included conditions relevant to potential applications such as refrigerated environments used for organ preservation,[31] as well as elevated temperatures where thermal ablation processes[32] may occur. At lower temperatures, the UCL lifetime remained virtually unchanged, while at 50 °C, a slightly more pronounced, though still moderate, decrease in lifetime was observed, indicating stable sensor performance across a broad thermal range.

To assess the robustness of the nIM against small variations in UCNP properties, primarily arising from batch-to-batch variability, we compared the UCL decay curves obtained from the originally used UCNPs with those from a slightly different batch. These new nanoparticles featured a thinner CaF_2 shell and a slightly higher Tm^{3+} doping concentration (1% instead of 0.5%). The results, presented in Figure S8 (Supporting Information), show that the resulting UCL lifetimes are nearly identical, with variations well within the experimental uncertainty associated with the lifetime determination. This confirms that the performance of the nIM is not significantly affected by minor changes in the UCNP synthesis parameters. In addition, we verified the long-term stability of the nIM by evaluating the calibration curve over time. Specifically, we measured the UCL lifetime as a function of excitation irradiance for two independent calibration curves acquired five weeks apart (Figure S9, Supporting Information). The results demonstrate excellent consistency, confirming the reliability of the nIM over extended periods.

2.3. Theoretical Interpretation

To shed light on the nature of the irradiance-dependent lifetime phenomenon leading to the nIM, we performed a rate equation analysis. We theoretically reproduced the experimental behavior of the UCL lifetime with the excitation laser irradiance using the following rate equation model:

$$
\begin{aligned}
\frac{dN_{Yb1}}{dt} &= -W_{Yb1}N_{Yb1} + \frac{1}{2}W_{Yb1}\frac{I}{I_{sat}}\left(N_{Yb0} - N_{Yb1}\right) - K_{ET1}N_{Tm0}N_{Yb1} \\
&\quad - K_{ET2}N_{Tm1}N_{Yb1} - K_{ET3}N_{Tm2}N_{Yb1}\ , \\
\frac{dN_{Tm1}}{dt} &= -W_{Tm1}N_{Tm1} + W_{Tm21}N_{Tm2} + W_{Tm31}N_{Tm3} \\
&\quad + K_{ET1}N_{Tm0}N_{Yb1} - K_{ET2}N_{Tm1}N_{Yb1}\ , \\
\frac{dN_{Tm2}}{dt} &= -W_{Tm2}N_{Tm2} + W_{Tm32}N_{Tm3} + K_{ET2}N_{Tm1}N_{Yb1} \\
&\quad - K_{ET3}N_{Tm2}N_{Yb1}\ , \\
\frac{dN_{Tm3}}{dt} &= -W_{Tm3}N_{Tm3} + K_{ET3}N_{Tm2}N_{Yb1}
\end{aligned}
\tag{4}
$$

N_{Tmj} is the density of Tm^{3+} ions in the energy level j, where the subscripts $j = 0, 1, 2, 3$ represent the $^3H_6$, $^3F_4$, $^3H_4$, $^1G_4$ energy levels of Tm^{3+} ions, respectively (see **Figure** 4A). The populations of levels with faster decay rates, such as $^3H_5$, $^3F_2$, and $^3F_3$, were neglected or assumed to be in thermal equilibrium with the corresponding lower levels. Therefore $N_{Tm0} + N_{Tm1} + N_{Tm2} + N_{Tm3} = N_{Tm}$, where N_{Tm} represents the total density of Tm^{3+} ions in the nanoparticle. On the other hand, N_{Yb0} and N_{Yb1} are the Yb^{3+} ions density in the $^2F_{7/2}$ and $^2F_{5/2}$ energy levels, respectively ($N_{Yb0} + N_{Yb1} = N_{Yb}$, with N_{Yb} being the total density of Yb^{3+} ions in the nanoparticle). W_{Tmjl} is the decay rate from Tm^{3+} level j to level l whereas W_{Tmj} is the total decay rate of the energy level j of Tm^{3+} ions. The decay rate of Yb^{3+} ions is W_{Yb1}. These decays rates can include a radiative component, particularly from the transitions of excited levels to the ground state, as well as a non-radiative component due to multi-phonon relaxation, surface effects, and defects within the nanoparticle. On the other hand, K_{ET1}, K_{ET2}, and K_{ET3}, are the coefficients of the resonant energy transfer from the excited Yb^{3+} ion (sensitizer) to levels 1, 2, and 3 of the Tm^{3+} ion (activator), respectively (see Figure 4A). The excitation laser irradiance or power density is denoted by I (in W cm^{-2}). This value was normalized by the saturation irradiance $I_{sat} = \hbar\omega W_{Yb1}/(2\sigma_{Yb1})$ of the Yb^{3+} transition, where σ_{Yb1} is the corresponding absorption (approximately equal to the emission) cross-section at the laser wavelength, and $\hbar\omega$ represents the transition energy, resonant with the excitation laser wavelength. For the simulations, we initially used decay rates, energy transfer coefficients, and other physical parameter values of a similar order of magnitude to those reported in the literature.[33–36] These parameters were then fine-tuned to match our experimental results (Section S10, Supporting Information).

To theoretically study the behavior of the UCL lifetime, we analyzed the time evolution of the populations by considering a pulsed excitation laser with a square temporal profile with a pulse width of 10 ms, in agreement with the experiments. At the initial time $t = 0$, when the laser is switched on, all ions are in their ground state, leaving the excited levels initially unpopulated. Therefore, the initial conditions for the simulations at $t = 0$ are $N_{Tm1} = N_{Tm2} = N_{Tm3} = N_{Yb1} = 0$, $N_{Tm0} = N_{Tm}$, and $N_{Yb0} = N_{Yb}$. We numerically solved Equation (4) using an explicit Runge-Kutta method in Matlab.[37] Specifically, the time evolution of the N_{Tm2} population after the laser is switched off (at $t =$ 10 ms) defines the UCL decay curve of the NIR band. As an example from the simulation, Figure 4B shows the time evolution of the excitation laser irradiance, $I(t)$, and the population $N_{Tm2}(t)$ for a low irradiance of $I = 50$ W cm^{-2}, corresponding to $I/I_{sat} \simeq 0.003$. Here, the decay curve of the N_{Tm2} population, responsible for the 770 nm UCL, has a decay time of 266 µs. Another example, shown in Figure 4C, depicts the case for a high irradiance of $I = 10$ kW cm^{-2} (corresponding to $I/I_{sat} \simeq 0.6$), where N_{Tm2} display a significant longer decay time of 1116 µs. The simulated UCL lifetime as a function of laser irradiance is shown in Figure 4D

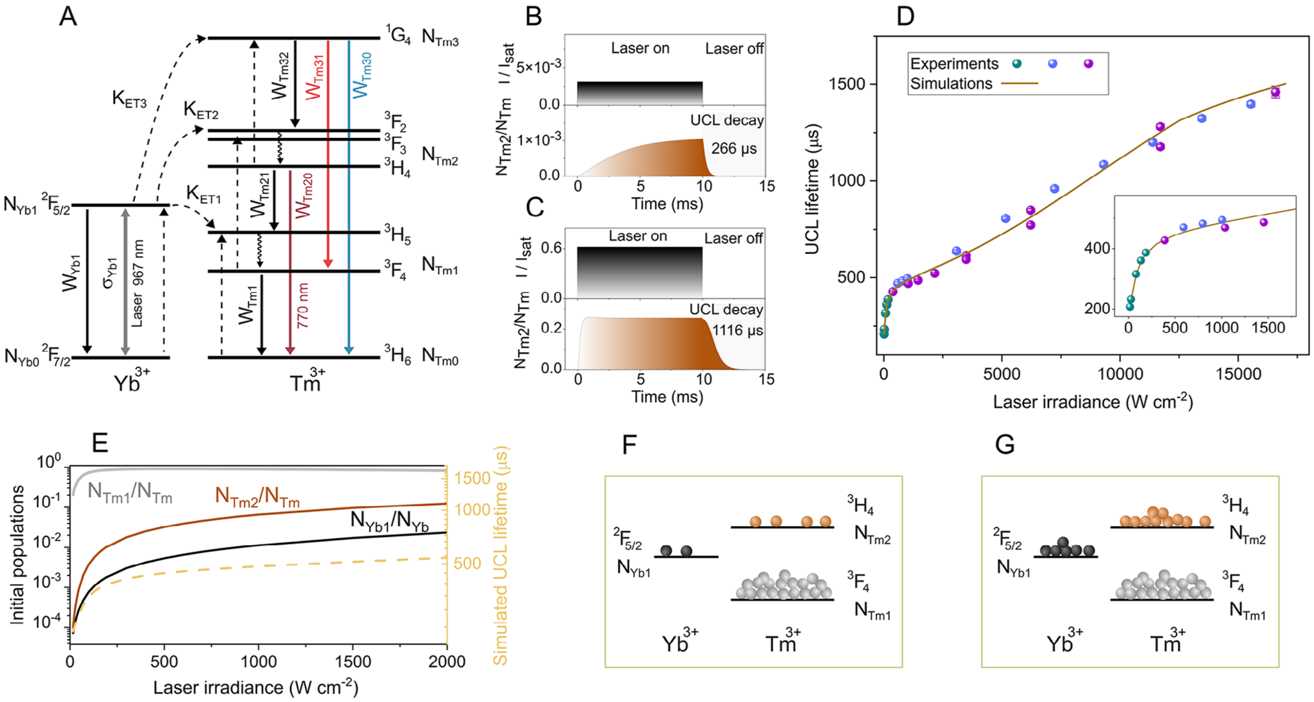

Figure 4. A) Energy-level diagram for Yb^{3+} and Tm^{3+} ions describing all the physical processes used in the rate equation model. Black dashed lines represent the Yb →Tm energy transfer mechanism (K_{ET1}, K_{ET2}, K_{ET3}). Gray solid line represents ground state absorption (and stimulated emission) of Yb^{3+} ions (σ_{Yb1}). The rest of solid lines represent decay rates from different levels. Faster non-radiative decay rates are represented by wavy lines. B) and C) Representative schematic of a developed simulation for two different laser irradiances: B) a low irradiance $I/I_{sat} = 0.003$ ($I = 50$ W cm^{-2}) and C) a high irradiance $I/I_{sat} = 0.6$ ($I = 10$ kW cm^{-2}). In each graph we represent the time evolution of the excitation laser with 10 ms pulse width and the time evolution of the population N_{Tm2} corresponding to level $^3H_4$ of Tm^{3+} ions. D) Simulated (solid line) UCL lifetime as a function of the excitation laser irradiance. Symbols are the experimental data from Figure 3H. The inset shows the low irradiance range. E) (left axis) Normalized initial populations of the excited energy levels for Tm^{3+} and Yb^{3+} ions at the end of the laser pulse, as a function of the laser irradiance. (right axis) Simulated UCL lifetime versus the excitation irradiance (dashed line). F,G) Diagram illustrating the population of excited Yb^{3+} and Tm^{3+} levels at the end of the excitation pulse for low (F) and high (G) irradiance levels.

(solid curve) along with the experimental data from the different experiments carried out (data from Figure 3H), demonstrating strong agreement with the experimental results (symbols). An inset in Figure 4D better shows the low irradiance regime. This good agreement suggest that the irradiance-dependent UCL lifetime phenomenon can be effectively described as a matter of population dynamics. This approach creates a range of possibilities for linking the luminescent emission of complex systems, like UCNPs, with measurable external factors.

We utilized the theoretical model to better understand the mechanism behind the irradiance-dependent UCL lifetimes. The key aspect is how the various energy levels of Tm^{3+} and Yb^{3+} ions are populated based on the laser irradiance. We then examined how the initial populations for the decay regime, that is, the populations reached at the end of the laser pulse, change with the excitation laser irradiance. These initial populations serve as the starting point from which the relaxation of the system occurs. The results are shown in Figure 4E. For comparison, the simulated UCL lifetime as a function of laser irradiance is also plotted (right axis). The initial population of the energy levels changes with laser irradiance but in a distinct manner, thereby influencing the contributions of various mechanisms to the UCL lifetime. As general trend, the first excited level of Tm^{3+} ions ($^3F_4$) remains highly populated and quickly saturates with increasing excitation irradiance (see N_{Tm1} in Figure 4E). At low irradiance levels, the other excited energy levels remain nearly unpopulated, as illustrated in the scheme in Figure 4F. In this configuration, with most of the population concentrated in the ground or lower energy states, a shorter lifetime is observed. As laser irradiance increases, the population of the $^2F_{5/2}$ level in Yb^{3+} ions and, to a greater extent, the $^3H_4$ level in Tm^{3+} ions become more significant relative to the $^3F_4$ level in Tm^{3+} (as shown in the scheme in Figure 4G). These additional contributions appear to lengthen the UCL decay time. Furthermore, the observed behavior of the UCL lifetime with increasing laser irradiance (initially rising rapidly and then transitioning to a nearly linear trend) seems to be related to changes in the initial populations of the $^2F_{5/2}$ level in Yb^{3+} ions and the $^3H_4$ level in Tm^{3+} ions (see Figure 4E). As the excitation irradiance increases, these two initial populations begin to saturate, leading the UCL lifetime to shift into a different regime.

2.4. Verifying Sensor Performance in Various Media

In order to explore the potential of the developed sensor, we tested the nIM under complex scenarios, where the excitation beam is modified when propagating through different media before reaching the nIM. We prepared a phantom sample

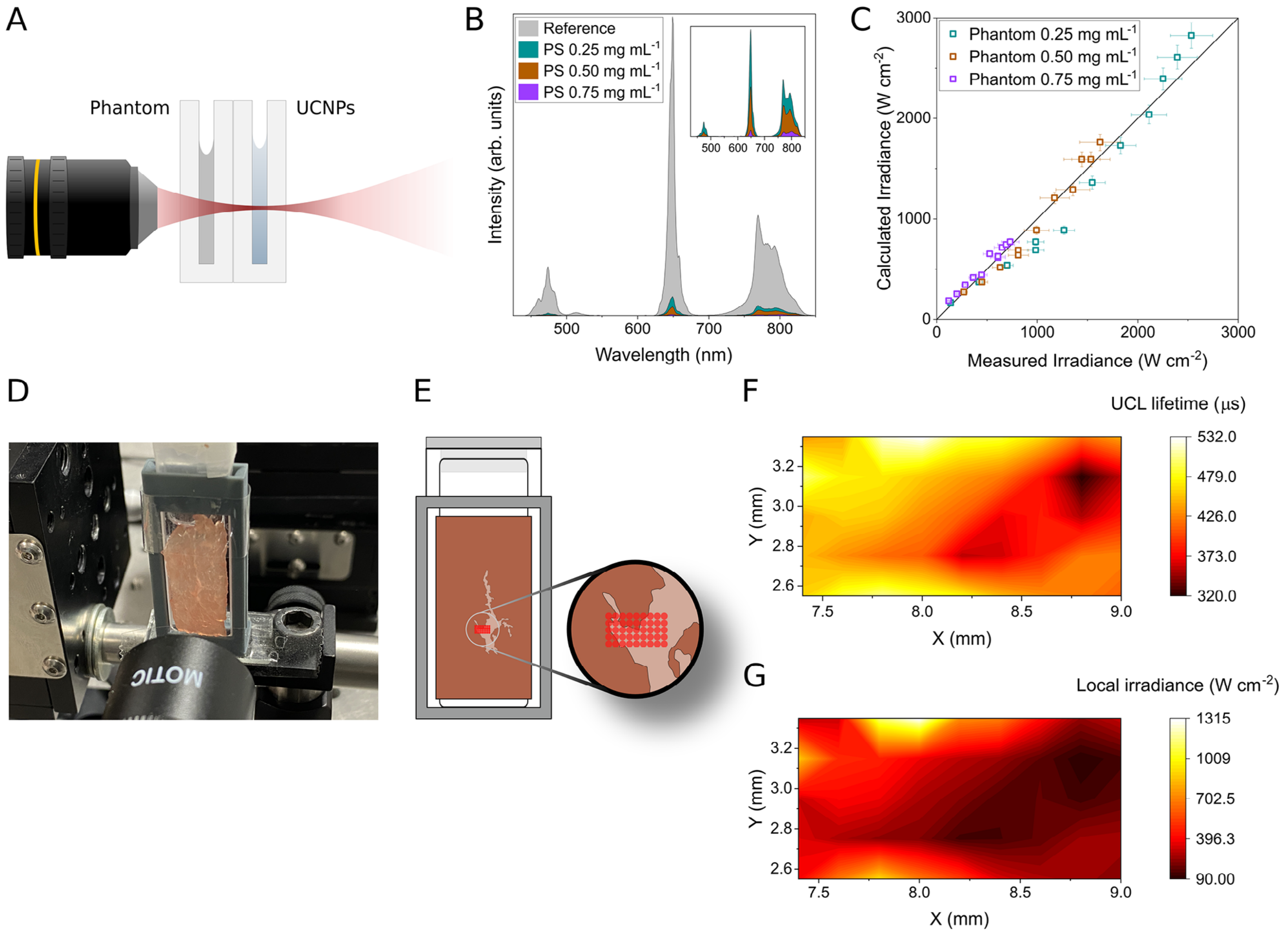

Figure 5. A) Schematic of the experimental setup for measuring the UCL lifetime through an aqueous dilution of 1 µm diameter polystyrene spheres B) UCL esmission spectra collected from UCNPs without a phantom (gray reference) and from UCNPs with phantoms interposed in front at three different concentrations (0.25, 0.50, and 0.75 mg mL^{-1}) C) The plot shows the irradiance derived from the UCL lifetime calibration curve (calculated irradiance) versus the irradiance measured at the exit of the cuvette filled with the phantom, accounting for laser power and spot size. D) Photograph of the experimental setup used to measure spatially resolved UCL through biological tissue. E) Schematic representation of the analyzed tissue area, showing the corresponding UCL lifetime (F) and irradiance (G) maps.

using an aqueous solution of highly monodisperse 1 µm diameter polystyrene spheres (Microparticles GmbH). The phantom sample was placed in a 1 mm-optical-path cuvette, positioned directly in front of the cuvette containing the UCNPs (see schematic in **Figure** 5A). Three different concentrations of polystyrene spheres (0.25, 0.50, and 0.75 mg mL^{-1}) were selected to provide a good signal-to-noise ratio for measuring UCL decay curves, while closely mimicking the scattering coefficients of tissues such as the bladder and muscle.[38] In order to quantify the decrease in the luminescence due to the scattering within the phantom sample, we first analyzed the UCL emission spectrum. As expected, this reduction is more pronounced in the blue and red bands, while the near infrared region is less affected (see Figure 5B). In particular, the luminescence measured through the phantom sample with the lowest concentration shows a decrease by a factor of 20 in the blue band, 14 in the red band, and 9 in the infrared band. This phenomenon is attributed to a combination of a decrease in excitation irradiance (see spot size data in Section S11, Supporting Information) and a reduction in collected luminescence, which varies depending on the emission band (see data in Section S12, Supporting Information). This observation is the primary reason for our focus on the band with maximum at 770 nm as the most suitable one for monitoring local irradiance in complex media.

For each phantom, we measured the UCL lifetime across a range of laser excitation irradiances, keeping the positions of both the phantom and UCNP sample cuvettes fixed while varying the laser's output power. By interpolating data points from the sensor's calibration curve, we calculated the irradiance reaching the nanoparticles locally, which corresponds to the readout of our nIM. To validate the accuracy of our irradiance estimation, we measured the laser beam's irradiance exiting the phantom sample cuvette by temporarily removing the UCNP sample cuvette. This measured irradiance was then plotted against the calculated irradiance derived from the UCL lifetime calibration curve in Figure 5C. Higher phantom concentrations reduce the maximum achievable local excitation irradiance. Most notably, the close agreement between the calculated and measured values (as shown by the data aligning with the solid line in Figure 5C) confirms the accuracy of the nIM and the robustness of the calibration. This result demonstrates that the actual irradiance reaching the target region, where the UCNPs are located, can be precisely determined by remotely measuring their time-resolved UCL.

To simulate a real-life scenario involving biological tissues and demonstrate the potential of our nIM, we spatially resolved the UCL lifetime measurements through a heterogeneous medium. The selected tissue was a carpaccio beef cut, consisting of a fat layer surrounded by regions with higher muscle fibers content. The tissue was adhered to the surface of the UCNP sample cuvette, as shown in Figure 5D. Due to its heterogeneous 3D structure and composition, the tissue caused a spatially dependent attenuation of the excitation irradiance. By scanning the tissue across the laser beam, we generated a spatial map of UCL lifetimes, which subsequently allowed us to create a corresponding map of the laser beam local irradiance distribution at the UCNP sample, located behind the tissue. As the laser spot diameter is approximately 200 µm, we performed the scan in increments of 200 µm in both the vertical and horizontal directions. The scanned region covered 0.8 mm vertically and 1.6 mm horizontally, yielding 45 measurement points (see Figure 5E). Figure 5F,G show the UCL lifetime map and irradiance map, respectively. When the irradiance map is superimposed on the examined tissue region, areas of lower irradiance correspond closely to regions where fat is more concentrated (i.e., more scattering is generated), consistent with the visual appearance of the tissue. Examining the irradiance values in Figure 5G, we note that within a spatial region of about a millimeter, our target zone shows local irradiance levels between 100 and 1300 W cm^{-2}, corresponding to a variation of one order of magnitude. This highlights the importance of monitoring local irradiance to ensure reproducible and effective results, particularly in biological applications. This experiment reveals the potential of nIMs not only for monitoring and adjusting irradiance but also for mapping tissues to identify more transparent regions where excitation irradiance is less attenuated, thereby minimizing light dosage. Importantly, these findings address a major challenge in nanothermometry: the difficulty of correlating temperature measurements in complex media with calibrations performed under controlled conditions. For example, reliable nanothermometry methods like luminescence intensity ratio (LIR) nanothermometry often face inaccuracies in tissues.[39,40] This arises from the unpredictable attenuation of the excitation source when propagating through these media, and the subsequent bias on the temperature readout as a consequence of the irradiance-dependent response of the nano-thermometer. In addition, the fact that the luminescence lifetime from some lanthanide energy levels can be affected by irradiance, as demonstrated in this and other works, suggests that caution must be taken when designing lifetime-based nanothermometers, which are currently regarded as one of the most reliable nanothermometry methods for in vivo applications.[7,23,25,26,41] As a consequence, knowing the local irradiance is required to deduce the LIR-to-temperature or lifetime-to-temperature calibration curve that is needed to accurately deduce the local temperature. In this work, we have demonstrated that certain lanthanide-doped nanoparticles, such as the UCNPs proposed here, can feature a specific emission whose luminescence lifetime is only dependent on the incident irradiance, as it is negligibly dependent on temperature (Figure S6, Supporting Information). Thus, the incorporation of this technology to nanothermometers may serve as a robust way to measure local irradiance, permitting to select the correct nanothermometric calibration to accurately and remotely monitor local temperatures in complex media.

3. Conclusion

In this work, we have developed a novel wireless nano irradiance sensor capable of adapting to any shape and providing direct and remote irradiance readings. Based on upconversion lifetime measurements, this nano irradiance meter (nIM) is composed of $SrYb^{3+}F_5{:}Tm^{3+}_{0.5\%}@CaF_2$ UCNPs and offers multiple advantages over pre-existing powermeters such as i) giving direct readouts of local irradiance, foregoing the need of calculating the illuminated area, ii) providing robust luminescence feedback due to the blinking, photobleaching and autofluorescence-free upconversion nature of the emission, iii) enabling the measurement of local irradiance within the BW-I through a robust magnitude such as luminescence lifetime that is proven, in this case, to be independent from temperature, iv) having a fluid nature that enables it to adopt different shapes, as well as to diffuse and be potentially applied in sub-micrometric compartments or porous, heterogeneous and complex media.

We characterized the performance of the wireless nIM by analyzing the UCL lifetime of the 770 nm emission band of Tm^{3+} ions as a function of the excitation laser irradiance at 967 nm. The nanosensor operates over a range spanning more than three orders of magnitude in irradiance, initially displaying a rapid increase followed by a nearly linear trend. A relative irradiance sensitivity of 0.9% W^{-1} cm^2 was achieved at low irradiance levels, while a sensitivity of 0.008% W^{-1} cm^2 was obtained at higher irradiance values. These values represent an improvement over previously reported relative irradiance sensitivities based on luminescence ratiometric approaches. The theoretical interpretation proposed for the observed nIM behavior permitted to explain and accurately describe the experimental results, by properly fitting the luminescence lifetime versus irradiance calibration curve. Finally, the application of the nIM under realistic conditions enabled the creation of a 2D map of local irradiances, allowing for the remote and non-invasive identification of sub-millimetric regions of increased transparency in a real tissue for the first time. Thus, the proposed nIM stands out as a very interesting probe to monitor local irradiance and identify regions of interest during specific applications, but also as a potential tool to be incorporated into current nanothermometers to enable their in situ irradiance calibration when applied in complex media.

4. Experimental Section

Chemicals: Ytterbium (III) oxide (Yb_2O_3, 99.9%), thulium (III) oxide (Tm_2O_3, 99.9%), 1-octadecene (ODE, 90%), oleic acid (OA, 90%), oleylamine (OLA, 70%), strontium carbonate ($SrCO_3$, 99.9%), calcium carbonate ($CaCO_3$, 99.99%), trifluoroacetic acid (99%), n-hexane (95%), toluene (99.9%), ethanol absolute (EtOH).

Synthesis of $SrYbF_5{:}Tm^{3+}$ UCNPs Cores: The synthesis of the $SrYbF_5{:}Tm^{3+}$ UCNPs was performed following a slightly modified recipe of Fisher et al. via the thermal decomposition of the corresponding trifluoroacetates.[28] For a 1 mmol scale synthesis, 195 mg of Yb_2O_3 (0.4975 mmol), 2 mg of Tm_2O_3 (0.0025 mmol), and 147 mg of $SrCO_3$ (1 mmol) in 10 mL of H_2O and 2 mL of TFA (added drop by drop to avoid CO_2 burst), which was heated-up to 90 °C in a 100 mL three-neck flask connected to a condenser and kept at this temperature until a transparent solution was obtained. At this point, the solution was evaporated yielding a white solid powder that was dried under vacuum using a Schlenk line, and finally dissolved in a mixture of 6 mL of OA, 13 mL of 1-ODE, and 2 mL of OM that were added to the flask to dissolve the precursors. The mixture was then heated to 120 °C under vacuum using a Schlenk line. The cycle between Ar and vacuum was repeated three times. Subsequently, the solution was placed under an Ar atmosphere and heated to 300 °C at a rate of 20 °Cmin^{-1} and kept at this temperature for 1 h. After removing the heating, the mixture was left to cool down to RT naturally and the UCNPs were subsequently precipitated by the addition of 20 mL of EtOH and centrifuged at 4000g. The supernatant was discarded and the UCNPs were dispersed in 1 mL of n-hexane, and 8 mL of absolute EtOH were added before centrifugation at 3000g. The core UCNPs were then dispersed and preserved in 10 mL of n-hexane.

Core Enlargement: 2 mL of the washed cores solution were introduced into a 100 mL three-neck flask containing 3 mL of OA and 6 mL of ODE. After heating up the solution at 65 °C, this was carefully evacuated using a Schlenk line to evaporate the n-hexane. The flask was heated to 120 °C under vacuum using a Schlenk line and cycled three times with Ar. Finally the temperature of the solution was raised to 270 °C, and the shelling solution was added by dropwise injection through a septum using a syringe pump. The shell precursor solution was prepared by mixing the Ln-TFA (Yb/Tm same as used for the cores) and the Sr-TFA solid to a solution with a total amount of 4 mL OA and 8 mL 1-ODE. The shell precursor was injected at a rate of 12.2 mLh^{-1}. After injecting the precursor solution, the flask was maintained at 300 °C for an additional 10 min. After this time the heating was removed allowing the solution to cool down to RT. The samples were then precipitated by adding ethanol and centrifuged at approximately 4000g for 10 min. The supernatant was discarded, the solid dispersed in n-hexane, then precipitated in absolute EtOH, and finally collected via centrifugation at 4000g before being dispersed in 10 mL of n-hexane.

Core-Shell Synthesis With CaF_2 Shell: 5 mL of the washed cores were introduced in a 100 mL 3-neck flask and 2 mL OA and 4 mL ODE were added. After heating up the solution at 65 °C, this was carefully evacuated using a Schlenk line. After n-hexane evaporation the flask was heated to 120 °C under vacuum using a Schlenk line and cycled three times with Ar. Finally the temperature of the solution was raised to 270 °C, and the shelling solution was added by dropwise injection through a septum using a syringe pump. At 270 °C dropwise injection of the CaF_2 shell precursor solution (12 mL at 0.16 mM) was started through a septum using a syringe pump. The shell precursor solution was injected with a rate of 6.0 mLh^{-1}. After the desired precursor solution was injected the flask was kept at 300 °C for another 10 min before removing the heating mantle and cooling down to room temperature. The samples were precipitated with addition of absolute EtOH and centrifuged at approximately 10000g. Samples were washed three times by dispersing in n-hexane, precipitating in ethanol, and collecting via centrifugation before finally dispersing in toluene.

Morphological Characterization: High resolution TEM (HR-TEM) and high-resolution scanning TEM (HR-STEM) in HAADF images were obtained using a FEI Talos F200X working at 200 kV and coupled to a CMOS Ceta 16M digital camera. Samples were prepared by depositing a drop of UCNPs dispersion onto a carbon-coated copper grids and dried at RT.

Optical Characterization: Luminescence lifetimes were determined using the time-resolved photon counting method with a custom-built fluorescence system, as previously described.[42] The beam from a 967 nm pigtailed 10 W continuous wave (CW) excitation laser (JDSU, L4-9897603), which was equipped with both current and temperature controllers (ILX Lightwave, LDX-36025-12, and LDT-5525B, respectively), passes through a long-pass dichroic filter (Thorlabs, DMLP900R). It was then focused onto a micro-cuvette (Starna Scientific 1/Q/1, 1 mm optical path) using a 10x objective. The luminescence emitted by the sample was directed by the dichroic mirror to a short-pass filter, which effectively blocks reflected radiation in the range of 860 to 1500 nm (Thorlabs, FESH0850). The filtered beam was then focused into an optical fiber connected to a monochromator (Horiba Jobin Yvon, iHR320). This monochromator utilized a grating with 1200 grooves per mm, along with a photomultiplier tube (Hamamatsu, R928) for measuring the upconversion luminescence.

The laser controller could operate the laser in CW mode for steady-state luminescence measurements and also produce excitation pulses ranging from 40 µs to the millisecond scale. The rise and fall times of the laser were significantly shorter (nominally below 10 µs) than the observed UCL decay times. The photomultiplier tube that detects the luminescence signal was connected to a 50 Ohm input of a digital oscilloscope (Agilent, DSO9104A), with the signal from the laser controller serving as the trigger. A custom Matlab program was used to analyze each signal in real-time, directly from the oscilloscope. This code could emulate both the discriminator and the multichannel counter functions.[43] After procesing over 5000 trigger signals, a luminescence decay curve was generated. The luminescence lifetime was then extracted by fitting these decay curves to a single exponential function. For this fitting process, a time window from t_{ini} to t_{end} was defined, where t_{end} was selected to be sufficiently long to capture the complete decay of the luminescence (typically t_{end} equal or larger than 5 ms). For each experimental decay curve, approximately 25 fits were performed, varying the initial fitting time t_{ini} within the range where the luminescence signal intensity decreases from 85% to 75% of its maximum value (Figure S11, Supporting Information). This fitting procedure yields an average lifetime along with its standard error. To further estimate the experimental uncertainty in determining the UCL lifetime, long-term stability measurements were conducted under constant experimental conditions at three representative irradiance levels. A conservative 1% uncertainty across all irradiance values was adopted. The final uncertainty for each data point was determined by comparing this 1% benchmark with the standard error derived from the lifetime fitting procedure; the larger of the two values was then used.

To characterize the laser irradiance at the sample position, the laser power was measured using a thermal sensor power meter (Thorlabs, S310C) and determined the beam size with the knife-edge technique[30] employing a highly sensitive germanium sensor (Thorlabs, S122B).

Supporting Information

Supporting Information is available from the Wiley Online Library or from the author.

Acknowledgements

This work was supported by the Ministerio de Ciencia e Innovación (PID2023-150645OA-I00, PID2021-122806OB-I00, TED2021-132317B-I00), Fundación Familia Alonso (2024/0041), and Comunidad de Madrid (P2022/BMD-7403 RENIM-CM). A.C.R. thanks UCM-Santander for a predoctoral contract (CT15/23). J.P.C. acknowledged support from the Comunidad de Madrid, Spain, through an "Atracción de Talento Investigador" fellowship (2022-T1/BMD-23751). TOC figure was partially created with BioRender.com.

Conflict of Interest

The authors declare no conflicts of interest.

Data Availability Statement

The data that support the findings of this study are available from the corresponding author upon reasonable request.

Keywords

lifetime, lanthanide nanoparticles, nanoirradiance meter, power meter, upconversion luminescence

Received: January 10, 2025
Revised: April 23, 2025
Published online:

---

[1] B. W. Pogue, J. T. Elliott, S. C. Kanick, S. C. Davis, K. S. Samkoe, E. V. Maytin, S. P. Pereira, T. Hasan, *Phys. Med. Biol.* **2016**, *61*, R57.

[2] J. C. Martins, A. Skripka, C. D. S. Brites, A. Benayas, R. A. S. Ferreira, F. Vetrone, L. D. Carlos, *Front. Photonics* **2022**, *3*, 1037473.

[3] M. M. Kim, A. Darafsheh, *Photochem. Photobiol.* **2020**, *96*, 280.

[4] L. Marciniak, M. Szalkowski, A. Bednarkiewicz, K. Elzbieciak-Piecka, *J. Mater. Chem. C* **2022**, *10*, 11040.

[5] C. Hernández-Álvarez, G. Brito-Santos, I. R. Martín, J. Sanchiz, K. Saidi, K. Soler-Carracedo, L. Marciniak, M. Runowski, *J. Mater. Chem. C* **2023**, *11*, 10221.

[6] P. Rodríguez-Sevilla, G. Spicer, A. Sagrera, A. P. Adam, A. Efeyan, D. Jaque, S. A. Thompson, *Adv. Opt. Mater.* **2023**, *11*, 2201664.

[7] C. D. S. Brites, R. Marin, M. Suta, A. N. C. Neto, E. Ximendes, D. Jaque, L. D. Carlos, *Adv. Mater.* **2023**, *35*, 2302749.

[8] T. Muñoz-Ortiz, L. Abiven, R. Marin, J. Hu, D. H. Ortgies, A. Benayas, F. Gazeau, V. Castaing, B. Viana, C. Chanéac, D. Jaque, F. E. Maturi, L. D. Carlos, E. Martín Rodríguez, J. G. Solé, *Part. Part. Syst. Charact.* **2022**, *39*, 2200100.

[9] Y. Shen, J. Lifante, N. Fernández, D. Jaque, E. Ximendes, *ACS Nano* **2020**, *14*, 4122.

[10] D. Mendez-Gonzalez, J. Lifante, I. Zabala Gutierrez, R. Marin, E. Ximendes, E. S. de Diego, M. C. Iglesias de la Cruz, F. J. Teran, J. Rubio-Retama, D. Jaque, *Nanoscale* **2022**, *14*, 16208.

[11] W. C. Vogt, J. K. Barton, A. Agrawal, T. J. Pfefer, *Measurement and Thermal Dependence of Biological Tissue Optical Properties*, John Wiley & Sons, Ltd, New York **2018**, pp. 355–378.

[12] V. K. Nagarajan, B. Yu, *Lasers Surg. Med.* **2016**, *48*, 686.

[13] E. M. Graham, K. Iwai, S. Uchiyama, A. P. de Silva, S. W. Magennis, A. C. Jones, *Lab Chip* **2010**, *10*, 1267.

[14] Y. Shen, J. Lifante, I. Zabala-Gutierrez, M. de la Fuente-Fernández, M. Granado, N. Fernández, J. Rubio-Retama, D. Jaque, R. Marin, E. Ximendes, A. Benayas, *Adv. Mater.* **2022**, *34*, 2107764.

[15] S. Kalytchuk, K. Poláková, Y. Wang, J. P. Froning, K. Cepe, A. L. Rogach, R. Zbořil, *ACS Nano* **2017**, *11*, 1432.

[16] P. Rodríguez-Sevilla, R. Marin, E. Ximendes, B. del Rosal, A. Benayas, D. Jaque, *Front. Chem.* **2022**, *10*, 941861.

[17] S. Gai, C. Li, P. Yang, J. Lin, *Chem. Rev.* **2014**, *114*, 2343.

[18] G. Chen, H. Qiu, P. N. Prasad, X. Chen, *Chem. Rev.* **2014**, *114*, 5161.

[19] S. Wu, G. Han, D. J. Milliron, S. Aloni, V. Altoe, D. V. Talapin, B. E. Cohen, P. J. Schuck, **2009**, *106*, 10917.

[20] Z. Zhu, *Anal. Chim. Acta* **2019**, *1054*, 122.

[21] J. Xu, J. Zhou, Y. Chen, P. Yang, J. Lin, *Coord. Chem. Rev.* **2020**, *415*, 213328.

[22] D. R. Gamelin, H. U. Gudel, in *Transition Metal and Rare Earth Compounds: Excited States, Transitions, Interactions II*, (Eds: H. Yersin), Springer, Berlin Heidelberg **2001**, pp. 1-56.

[23] Y. Han, C. Gao, T. Wei, K. Zhang, Z. Jiang, J. Zhou, M. Xu, L. Yin, F. Song, L. Huang, *Angew. Chem.-Int. Edit.* **2022**, *61*, 202212089.

[24] D. J. Gargas, E. M. Chan, A. D. Ostrowski, S. Aloni, M. V. P. Altoe, E. S. Barnard, B. Sanii, d J. J. Urban, D. J. Milliron, B. E. Cohen, P. J. Schuck, *Nat Nanotechnol.* **2014**, *9*, 300.

[25] A. Teitelboim, B. Tian, D. J. Garfield, A. Fernandez-Bravo, A. C. Gotlin, P. J. Schuck, B. E. Cohen, E. M. Chan, *J. Phys. Chem. C* **2019**, *123*, 2678.

[26] A. Casillas-Rubio, D. Mendez-Gonzalez, M. Laurenti, J. Rubio-Retama, O. G. Calderón, S. Melle, *Nanoscale* **2024**, *16*, 12184.

[27] F. E. Maturi, C. D. S. Brites, R. R. Silva, K. Nigoghossian, D. Wilson, R. A. S. Ferreira, S. J. L. Ribeiro, L. D. Carlos, *Adv. Photon. Res.* **2022**, *3*, 2100227.

[28] S. Fischer, C. Siefe, D. F. Swearer, C. A. McLellan, A. P. Alivisatos, J. A. Dionne, *Angew. Chem.-Int. Edit.* **2020**, *59*, 21603.

[29] L. Labrador-Páez, U. Kostiv, Q. Liu, Y. Li, H. Ågren, J. Widengren, H. Liu, *J. Phys. Chem. Lett.* **2022**, *13*, 11208.

[30] M. A. de Araújo, R. Silva, E. de Lima, D. P. Pereira, P. C. de Oliveira, *Appl. Opt.* **2009**, *48*, 393.

[31] E. Roussakis, J. P. Cascales, D. Yoeli, A. Cralley, A. Goss, A. Wiatrowski, M. Carvalho, H. B. Moore, E. E. Moore, C. A. Huang, C. L. Evans, *Sens. Diagn.* **2024**, *3*, 1014.

[32] S. Missios, K. Bekelis, G. H. Barnett, *Neurosurg. focus* **2015**, *38*, E13.

[33] Y. Liu, Y. Lu, X. Yang, X. Zheng, S. Wen, F. Wang, X. Vidal, J. Zhao, D. Liu, Z. Zhou, C. Ma, J. Zhou, J. A. Piper, P. Xi, D. Jin, *Nature* **2017**, *543*, 229.

[34] J. Wang, X. Sun, Y. Han, Z. Cheng, T. Liu, *Opt. Commun.* **2021**, *483*, 126663.

[35] Y. Han, J. Yang, Y. Deng, H. Hu, Z. Cheng, T. Liu, *Opt. Commun.* **2021**, *499*, 127305.

[36] V. Kale, M. Lastusaari, J. Hölsä, T. Soukka, *RSC Adv.* **2015**, *5*, 35858.

[37] J. R. Dorman P. J. Prince, *J. Comput. Appl. Math.* **1980**, *6*, 19.

[38] W. F. Cheong, S. A. Prahl, A. J. Welch, *IEEE J. Quantum Electron.* **1990**, *26*, 2166.

[39] M. Jia, M. Li, D. Li, X. Zhang, G. Chen, *Nano Lett.* **2024**, *24*, 15450.

[40] B. Zhang, X. Guo, Z. Zhang, Z. Fu, H. Zheng, *J. Lumines.* **2022**, *250*, 119110.

[41] M. Tan, F. Li, N. Cao, H. Li, X. Wang, C. Zhang, D. Jaque, G. Chen, *Small* **2020**, *16*, 2004118.

[42] S. Melle, O. G. Calderón, M. Laurenti, D. Mendez-Gonzalez, A. Egatz-Gómez, E. López-Cabarcos, E. Cabrera-Granado, E. Díaz, J. Rubio-Retama, *J. Phys. Chem. C* **2018**, *122*, 18751.

[43] T. Stacewicz, M. Krainska-Miszczak, *Meas. Sci. Technol.* **1997**, *8*, 453.